

Infragravity Wave Motions and Runup over Shallow Fringing Reefs

Okey Nwogu¹ and Zeki Demirbilek, F.ASCE²

Abstract: This paper presents the results of a combined laboratory and numerical investigation into the role of infragravity motions in the wave runup process over fringing coral reefs. Laboratory experiments were performed with a reef profile typical of fringing reef systems along the southeast coast of Guam. Spectral analysis of the measured time histories of surface elevation over the reef face and flats show significant changes to the wave energy spectrum shoreward of the break point. Most of the wave energy in the incident wave frequency band is dissipated within a few wavelengths of the reef face with the wave motions over the reef flat and shoreline dominated by oscillations at infragravity periods [O(100s) prototype]. The infragravity wave energy is minimum at the reef crest and increases as waves propagate shoreward over the reef flat and also with increasing water level on the reef. The dominant infragravity mode is the first reef oscillation mode with a wavelength approximately equal to four times the width of the reef flat. This component is resonantly amplified at the shoreline relative to the incident infragravity energy at the reef crest. A numerical model based on the Boussinesq equations is applied to the laboratory data and is able to describe complex changes to the wave spectrum over the reef flat due to nonlinear wave-wave interactions and wave breaking as well as runup at the shoreline.

DOI: 10.1061/(ASCE)WW.1943-5460.0000050

CE Database subject headings: Reefs; Ocean waves; Storm surges; Wave runup; Guam.

Author keywords: Coral reefs; Ocean waves; Long-period surges; Runup; Infragravity waves.

Introduction

Fringing reefs are shore-attached reefs characterized by shallow platforms that drop off sharply into deep water. In addition to providing habitat for a wide variety of marine organisms, fringing reefs also protect coastal areas from wave action. Due to the shallow water depth on the reef flat, most of the incident wave energy is dissipated by waves breaking on the frontal reef slope. However, extensive damage has occasionally been reported in low-lying coastal areas fronted by coral reefs during typhoon events (e.g., Ogg and Koslow 1978; Nakaza and Hino 1991; Jaffe and Richmond 1993). An improved understanding of the physics of wave inundation over reef systems is required to develop predictive models for hurricane/typhoon-emergency planning purposes and the assessment of hurricane/typhoon-induced erosion rates.

Waves propagating onto shallow fringing reefs undergo significant transformations due to nonlinear steepening, reflection from steep reef faces, wave breaking, bottom friction, and percolation over porous reef substrates. Field experiments by Lee and Black (1978) at Ala Moana Beach in Hawaii showed significant changes to the wave shape as the waves propagated over the reef. Waves breaking on the reef face reformed on the reef flat as steep

asymmetric borelike waves with multiple crests. Nonlinear wave-wave interaction effects led to the cross-spectral transfer of energy from the peak frequencies to lower and higher frequencies. The probability distribution of the sea surface elevation and heights over the reef flat was also significantly different from the Gaussian and Rayleigh distributions for linear waves.

Groups of waves breaking on the reef face also induce a time-varying setup of the mean water level over the reef flat. Early field observations by Munk and Sargent (1948) at Bikini Atoll in the Pacific Ocean showed the mean sea level over the platform reef was raised by 0.45 m to 0.6 m relative to the surrounding ocean. Laboratory investigations into the mean water level setup over reefs have been conducted by Gerritsen (1980), Seelig (1983), and Gourlay (1996a) among others. Seelig (1983) found that the setup increased with a wave energy flux parameter. The setup also increased as the water level over the reef flat decreased. Gerritsen (1980) and Gourlay (1996a) both described the nondimensional wave setup in terms of the relative water depth over the reef flat and a wave steepness parameter.

There have been a limited number of laboratory or field studies of wave runup on beaches fronted by fringing coral reef systems. The laboratory study by Seelig (1983) was one of the few that presented results of wave runup height, and noted differences between the runup characteristics of regular and irregular waves. Although regular waves induced a larger setup of the mean water level in the lagoon (ponding area between reef crest and shoreline), the maximum runup values were much higher in irregular sea states due to strong low-frequency oscillations in the lagoon and near the shoreline.

Infragravity wave oscillations have also been postulated to be responsible for the observed coastal damage along the reef coasts of Japan during typhoons (Nakaza et al. 1991). Infragravity waves could be trapped and resonantly amplified over the reef flat if the

¹Dept. of Naval Architecture and Marine Engineering, Univ. of Michigan, Ann Arbor, MI (corresponding author).

²Coastal and Hydraulics Laboratory, U.S. Army Engineer Research and Development Center, Vicksburg, MS.

Note. This manuscript was submitted on October 23, 2009; approved on January 13, 2010; published online on February 4, 2010. Discussion period open until April 1, 2011; separate discussions must be submitted for individual papers. This paper is part of the *Journal of Waterway, Port, Coastal, and Ocean Engineering*, Vol. 136, No. 6, November 1, 2010. ©ASCE, ISSN 0733-950X/2010/6-295-305/\$25.00.

infragravity wave period is close to one of the natural reef oscillation periods. It is imperative that predictive models for coastal flooding over reef-fronted coasts be able to describe low-frequency (infragravity) oscillations over the reef in addition to other hydrodynamic processes such as wave breaking, wave setup, wave reflection, bottom friction, percolation, breaking-induced currents, and wave-current interaction.

Numerical models based on the shallow water equations with a forcing term due to spatial gradients of the radiation stress (Longuet-Higgins and Stewart 1964) can be used to predict wave setup over coral reefs. A separate wave transformation model is required to determine breaking-induced changes to the wave height and the corresponding radiation stress gradients. Tait (1972) calculated the radiation stress gradient by assuming the post-breaking wave height to be a constant fraction of the water depth. The concept of a constant height to depth ratio becomes questionable for complex reef profiles given the wide range of observed values of wave height to water depth ratio. Gerritsen (1980) improved on this approach by solving the wave energy conservation equation with the breaking model of Battjes and Janssen (1978). Massel and Gourlay (2000) used an extended mild-slope equation for steep slopes to predict wave transformation across reef profiles. Wave breaking was parameterized using a modified form of the Battjes and Janssen (1978) breaking model. Symonds et al. (1995) noted that cross-reef currents could affect estimates of the water level setup and derived an analytical solution for the wave setup and cross-reef current over an idealized reef without a landward boundary.

Madsen et al. (1997) used a Boussinesq wave model to investigate infragravity wave motions over a planar beach profile, while Skotner and Apelt (1999) applied a Boussinesq model to a submerged coral reef. In contrast to mild-slope and spectral energy balance models, Boussinesq models are able to simultaneously describe short wave propagation, nonlinear energy transfer to infragravity modes, wave breaking, and breaking-induced currents. One major concern with applying Boussinesq models to fringing coral reefs is the relatively steep slope of the reef face, which may violate the underlying bottom-slope assumption of weakly dispersive models. Boussinesq equations are also solved on Eulerian grids and cannot simulate plunging overturning waves. Another concern is whether the parameterization of wave breaking in Boussinesq models can describe the release of bound infragravity waves as free waves at the break point as hypothesized by Longuet-Higgins and Stewart (1964).

In this paper, we present results from a combined laboratory and numerical model study of infragravity wave motions and wave runup over fringing reef profiles. Laboratory experiments were conducted with a reef profile typical of fringing reef systems along the southeast coast of Guam (Demirbilek et al. 2007). The water depths over the reef flat were smaller than characteristic height of the incident waves, leading to significant wave breaking and energy dissipation on the reef face. The postbreaking wave energy on the reef flat was dominated by long-period surges or infragravity waves with periods much longer than the incident wave periods. The minimum infragravity wave energy occurred at the reef crest and increased as the waves propagated shoreward over the reef flat. The water depth on the reef flat controlled the magnitude of infragravity wave energy in this region. Numerical simulations were conducted with a Boussinesq model to evaluate its ability to describe the observed wave breaking and reformation over the reef flat, nonlinear energy transfer to infragravity modes and the trapping of infragravity waves over shelf-type topography.

Description of Boussinesq Model

The Boussinesq model solves the depth-integrated mass conservation equation and exact dynamic free surface boundary equation expressed as a set of evolution equations for the free surface elevation $\eta(\mathbf{x}, t)$ and tangential velocity at the free surface $\mathbf{u}_s(\mathbf{x}, t)$ (e.g., McDonald and Witting 1984; Nwogu 2009)

$$\frac{\partial \eta}{\partial t} = -\nabla \cdot [(h + \eta)\bar{\mathbf{u}}] - \mu(\mathbf{x})\eta \quad (1)$$

$$\begin{aligned} \frac{\partial \mathbf{u}_s}{\partial t} = & -\nabla \left[g\eta + \frac{1}{2}\mathbf{u}_s \cdot \mathbf{u}_s - \frac{1}{2}w_\eta(1 + |\nabla\eta|^2) \right] - \mathbf{u}_\eta \times (\nabla \times \mathbf{u}_s) \\ & - \frac{1}{h + \eta} \nabla [v_t(h + \eta) \nabla \cdot \bar{\mathbf{u}}] - \frac{1}{2(h + \eta)} f_w \mathbf{u}_b |\mathbf{u}_b| - \mu(\mathbf{x})\mathbf{u}_s \end{aligned} \quad (2)$$

where $\bar{\mathbf{u}}$ =depth-averaged horizontal velocity; g =gravitational acceleration; h =seabed elevation; $(\mathbf{u}_\eta, w_\eta)$ =horizontal and vertical velocities at the free surface; v_t =eddy-viscosity coefficient for breaking-induced energy dissipation; and μ =quadratically varying Rayleigh damping coefficient that is used to absorb waves propagating out of the computational domain (Nwogu and Demirbilek 2001). The effect of a turbulent boundary layer at the seabed can be formally introduced by either modifying the bottom boundary condition (Liu and Orfila 2004) or as a shear stress in the depth-integrated momentum equation. Since we are using an equivalent momentum equation based on the tangential velocity at the free surface, an ad hoc dissipative term consistent with the quadratic drag-law parameterization in depth-integrated models is introduced to mimic the energy dissipation in the bottom boundary layer with f_w an equivalent bottom friction coefficient

The vertical profile of the flow field is required to close the system of equations. For weakly dispersive waves in shallow water, we approximate the velocity field with a second-order Taylor series expansion about an arbitrary elevation z_α in the water column (Nwogu 1993)

$$\begin{aligned} \mathbf{u}(\mathbf{x}, z, t) = & \mathbf{u}_\alpha + (z_\alpha - z)[\nabla(\mathbf{u}_\alpha \cdot \nabla h) + (\nabla \cdot \mathbf{u}_\alpha) \nabla h] \\ & + \frac{1}{2}[(z_\alpha + h)^2 - (z + h)^2] \nabla(\nabla \cdot \mathbf{u}_\alpha) \end{aligned} \quad (3)$$

$$w(\mathbf{x}, z, t) = -[\mathbf{u}_\alpha \cdot \nabla h + (z + h) \nabla \cdot \mathbf{u}_\alpha] \quad (4)$$

where $\mathbf{u}_\alpha(\mathbf{x}, t)$ =horizontal velocity at $z=z_\alpha$. Following Nwogu (1993), we choose $z_\alpha = -0.535(h + \eta)$ to minimize differences between the linear dispersion characteristics of the Boussinesq model and the exact dispersion relation for small amplitude waves. Given values of η and \mathbf{u}_s at any instant of time, \mathbf{u}_α is obtained by inverting a matrix equation derived from

$$\begin{aligned} \mathbf{u}_s = & \mathbf{u}_\eta + w_\eta \nabla \eta = \mathbf{u}_\alpha + (z_\alpha - \eta)[\nabla(\mathbf{u}_\alpha \cdot \nabla h) + (\nabla \cdot \mathbf{u}_\alpha) \nabla h] \\ & + \frac{1}{2}[(z_\alpha + h)^2 - (h + \eta)^2] \nabla(\nabla \cdot \mathbf{u}_\alpha) \\ & - [\mathbf{u}_\alpha \cdot \nabla h + (h + \eta) \nabla \cdot \mathbf{u}_\alpha] \nabla \eta \end{aligned} \quad (5)$$

The depth-averaged velocity and velocities at the free surface and seabed are then obtained from \mathbf{u}_α using

$$\begin{aligned} \bar{\mathbf{u}} = & \mathbf{u}_\alpha + \left[(z_\alpha + h) - \frac{(h + \eta)}{2} \right] [\nabla(\mathbf{u}_\alpha \cdot \nabla h) + (\nabla \cdot \mathbf{u}_\alpha) \nabla h] \\ & + \left[\frac{(z_\alpha + h)^2}{2} - \frac{(h + \eta)^2}{6} \right] \nabla(\nabla \cdot \mathbf{u}_\alpha) \end{aligned} \quad (6)$$

$$w_\eta = -[\mathbf{u}_\alpha \cdot \nabla h + (h + \eta) \nabla \cdot \mathbf{u}_\alpha] \quad (7)$$

$$\mathbf{u}_\eta = \mathbf{u}_\alpha + (z_\alpha - \eta)[\nabla(\mathbf{u}_\alpha \cdot \nabla h) + (\nabla \cdot \mathbf{u}_\alpha) \nabla h] + \frac{1}{2}[(z_\alpha + h)^2 - (h + \eta)^2] \nabla(\nabla \cdot \mathbf{u}_\alpha) \quad (8)$$

$$\mathbf{u}_b = \mathbf{u}_\alpha + (z_\alpha + h)[\nabla(\mathbf{u}_\alpha \cdot \nabla h) + (\nabla \cdot \mathbf{u}_\alpha) \nabla h] + \frac{1}{2}(z_\alpha + h)^2 \nabla(\nabla \cdot \mathbf{u}_\alpha) \quad (9)$$

The effect of wave breaking has been parameterized in the momentum equation [Eq. (2)] with an artificial eddy-viscosity-based dissipative term (e.g., Zelt 1991; Kennedy et al. 2000). This term is designed to reproduce the overall wave energy dissipation due to breaking but not the details of the turbulent motion. A conceptual breaking model is still required to define the onset of breaking and the postbreaking spatial and temporal evolution of the eddy viscosity. In this paper, we use an analogy to the idea initially introduced by von Neumann and Richtmyer (1950) to stabilize shocks in the Euler equations and later used by Smagorinsky (1963) to parametrize the effect of unresolved (subgrid-scale) processes on large-scale motions in an ocean circulation model and assume that the eddy viscosity is directly proportional to the horizontal gradient of the velocity at the wave front, i.e.,

$$v_i(\mathbf{x}, t) = B(\mathbf{x}, t) l_i^2 \left[\left(\frac{\partial u_\eta}{\partial x} \right)^2 + \left(\frac{\partial v_\eta}{\partial y} \right)^2 \right]^{1/2} \quad (10)$$

where l_i = characteristic length scale of the whitecaps and $B(\mathbf{x}, t)$ = breaking wave factor that varies from 0 to 1. The value of B is set to 1 if a wave is classified as breaking. The waves are assumed to start breaking when the horizontal component of the orbital velocity at the free surface, \mathbf{u}_η , exceeds 80% of the phase velocity of the waves, C , i.e.,

$$B = 1 \quad \text{if } |\mathbf{u}_\eta| \geq 0.8C \quad (11)$$

An advection-diffusion equation is solved for the spatial and temporal evolution of the wave breaking factor

$$\frac{\partial B}{\partial t} + \mathbf{u}_\eta \cdot \nabla B + v_\eta \frac{\partial B}{\partial y} = -\frac{\pi}{T_v} B + \sigma v \left(\frac{\partial^2 B}{\partial x^2} + \frac{\partial^2 B}{\partial y^2} \right) \quad (12)$$

where σ = empirical diffusion constant, T_v denotes a characteristic time scale over which the breaking factor decays to 4% of its initial value. The values of l_i , T_v , and σ are empirically chosen to fit measurements. For the simulations in this paper, we chose $T_v = 5T$ and $\sigma = 0.2$. The turbulent length scale, l_t , governs the overall rate of wave energy dissipation and is typically chosen to be of the order of the offshore wave height based on the observed correlation between the area of the whitecap region and square of the wave height (Svendsen 1984).

The evolution equations are integrated in time using a fourth-order Runge-Kutta method. The computational domain is discretized as a rectangular grid with uniform grid sizes Δx and Δy , in the x and y directions, respectively. The prognostic variables η and \mathbf{u}_s are defined at the grid points in a staggered manner with the surface elevation defined at the grid nodes while the velocities are defined half a grid point on either side of the elevation grid points. The spatial derivatives are evaluated using a central difference scheme. The matrix equation formed from Eq. (5) is inverted as a coupled set of tridiagonal equations for u_α and v_α along lines in the x and y directions, respectively. Waves propagating out of the domain are absorbed in damping or sponge layers placed at the boundaries of the computational grid.

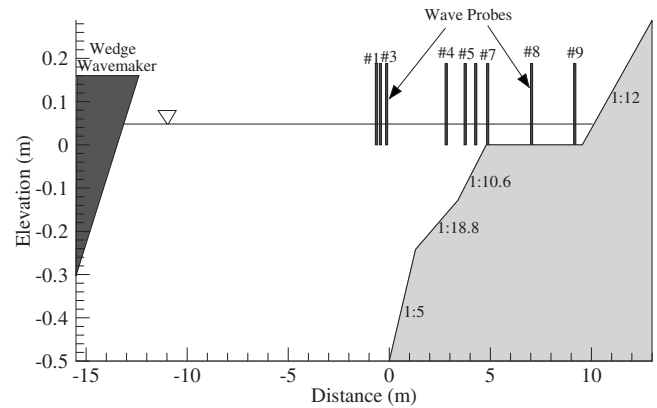


Fig. 1. Experimental setup

A simple but robust scheme is used to simulate the flooding and drying of computational cells. Initially dry cells are included in the computations when the total (potential and kinetic) energy head of any of the adjacent wet cells exceeds the elevation of the dry cell, i.e.,

$$\left[\eta + \frac{1}{2g} \mathbf{u}_s \cdot \mathbf{u}_s - \frac{1}{2g} w_\eta (1 + |\nabla \eta|^2) \right]_{\text{wet}} > -h_{\text{dry}} \quad (13)$$

To avoid instability issues associated with evaluating the bottom friction term in cells with extremely small water depths, a minimum depth criterion is applied to flooded cells. If the calculated water depth in any cell is less than a specified threshold, i.e., $h + \eta < \delta_{\text{min}}$, the cell is considered to be dry and excluded from the computations. The minimum depth criterion also works for receding waves.

One artifact of central difference finite-difference methods is the spurious ($2\Delta x$) oscillations introduced in regions with large gradients in the flow such as at the front of moving boundaries. These oscillations can be suppressed by spatial filtering (e.g., Madsen et al. 1997), implicit numerical diffusion (e.g., Kobayashi et al. 1987), or explicit numerical diffusion (e.g., Heitner and Housner 1970). In this paper, we adopt an explicit numerical diffusion method and choose the Smagorinsky-type formulation in which the artificial viscosity coefficient is proportional to the velocity gradient tensor and grid size

$$\nu = C_v^2 \Delta x \Delta y \left[(u_{\alpha,x})^2 + (v_{\alpha,y})^2 + \frac{1}{2} (u_{\alpha,y} + v_{\alpha,x})^2 \right]^{1/2} \quad (14)$$

A more detailed description of the numerical scheme is provided in Nwogo and Demirbilek (2001).

Laboratory Experiments

An idealized fringing reef was built in the two-dimensional wind-wave flume at the University of Michigan. The flume is 35 m long, 0.7 m wide, and 1.6 m high. The reef cross section consisted of a 1:12 beach followed by a 4.8-m-wide flat reef section and a composite-slope reef face as shown in Fig. 1. The cross-sectional profile of the reef face is similar to the one used in previous hydraulic model tests by Seelig (1983). However, a flat reef top was used in these experiments instead of the lagoon in Seelig (1983). The flat reef top is more representative of the reef systems along the southeast coast of Guam.

The reef surface was built using polyvinyl chloride plastic, a relatively smooth and impervious material. Although most natural

coral reefs are composed of hard calcium carbonate skeletal material and covered by a wide variety of benthic organisms, we felt that it would be too difficult to reproduce the hydraulic roughness and porosity of natural coral reefs in a laboratory setting. The experiments were designed to provide further insight into the physics of nonlinear wave transformation and runup over fringing reef profiles and data for validation of numerical models as opposed to model scale reproduction of hydrodynamic processes over natural coral reefs.

Irregular waves were generated in the tank with a plunger-type wavemaker. The toe of the reef slope was located at a distance of approximately 15.5 m from the wavemaker. Due to concern about the influence of re-reflected waves from the wavemaker, three capacitance wire wave gauges were installed in the constant depth section of the flume to quantify the amount of wave reflection. Six additional capacitance-wire wave gauges were used to measure the wave conditions across the reef profile as shown in Fig. 1. The wave gauges were located at distances of -1.11 , -0.92 , -0.59 , 2.75 , 3.68 , 4.22 , 4.8 , 6.97 , and 9.14 m from the toe of the reef. The wave gauges placed on the reef flat were designed to provide accurate measurements of wave setup over the reef flat. The bottom end of the gauges were inserted into holes drilled into the reef surface, allowing the gauges to record water level changes over the reef flat from an initially dry reef surface. A 1-m long capacitance-wire gauge was installed on the beach to measure runup.

Tests were run for a wide variety of irregular sea states with significant wave heights varying from 3 to 8.5 cm, spectral peak periods from 1 to 2.5 s, and water levels h_r from 0 to 5 cm on reef flat. Time histories of the water surface elevation were synthesized from JONSWAP spectral shapes with peak enhancement factor $\gamma=3.3$ using the random phase method. Linear theory was used to convert the water surface elevation to control signals for the wavemaker.

All gauges were zeroed before each test to minimize drift effects, data were collected for a duration of 900 s and sampled at 20 Hz. Data collection was initiated shortly after the wavemaker was started from initially calm water conditions. Further details on the experiments are provided in Demirbilek et al. (2007).

Results and Discussions

Laboratory Results

Typical recorded time histories of the surface elevation on the reef flat (Gauges 7–9) and the runup gauge are shown in Fig. 2 for incident waves with $H_{m0}=7.5$ cm, $T_p=1.5$ s, and $h_r=3.1$ cm. Most the waves broke violently on the reef face in a plunging manner, with a big splash-up as shown in Fig. 3. After breaking, the waves reformed on the reef flat as borelike waves with steep crest fronts and long flat trailing regions. Several types of bores were observed during the tests, ranging from non-breaking undular bores with multiple crests behind the bore front to fully turbulent bores with a turbulent roller region at its front. The bores evolved significantly as they traveled over the flat reef section with an increase in the long-period (infragravity) surge activity and a decrease in height of the short-period oscillations. Since the bore propagation speed is related to bore height, larger bores propagated faster, overtaking smaller bores. Offshore propagating bores were also observed. The onshore and offshore propagating bores appeared to cross each other without any visible interaction except for occasional breaking.

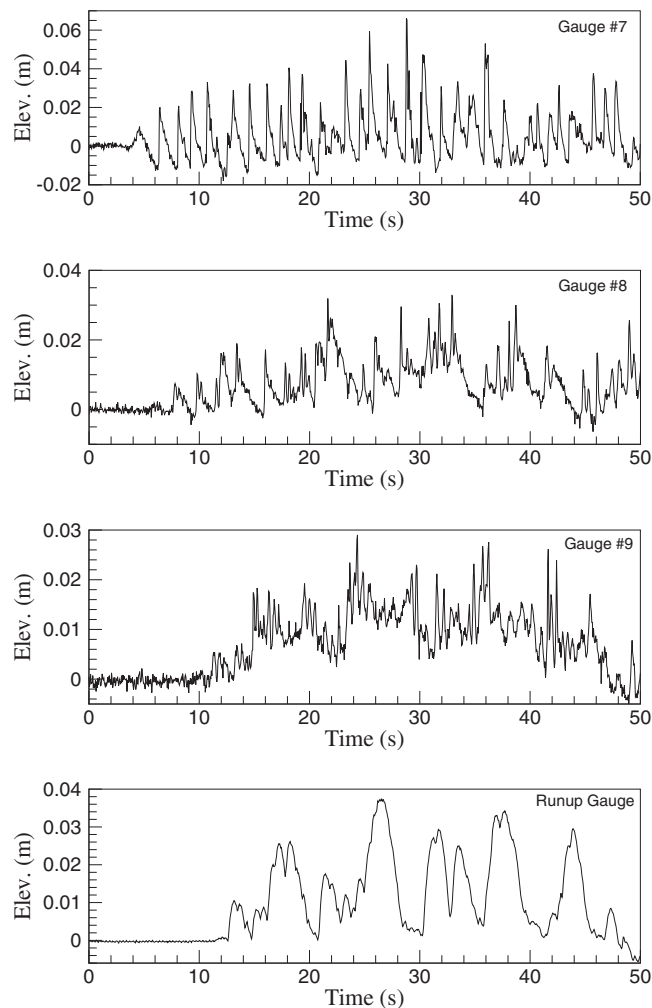


Fig. 2. Time series at runup gauge and reef flat Gauges 7–9 for incident waves with $H_s=7.5$ cm, $T_p=1.5$ s, and $h_r=3.1$ cm

Spectral densities of the water surface elevation were obtained by Fourier transforming the last 800 s of the time records and band-averaging 30 frequency components, resulting in 60 spectral degrees of freedom (dof) at a frequency resolution of 0.02 Hz. The spectral densities at offshore (Gauge 2) and reef face Gauges 5 and 6 are plotted in Fig. 4. The wave spectrum at the offshore gauge contains a relatively small amount of long-period energy which could be partially due to spurious long waves being generated at the wavemaker to compensate for the linear wavemaker



Fig. 3. Plunging breaking waves near reef crest

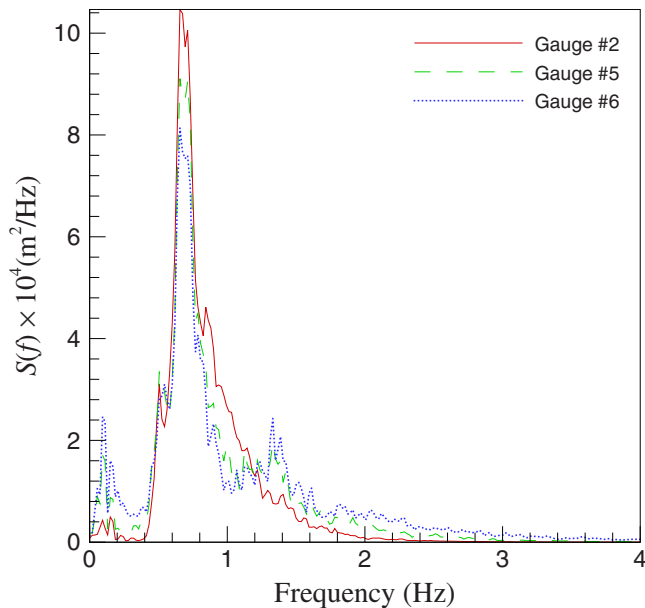


Fig. 4. Wave energy spectra at Gauges 2, 5, and 6 for incident waves with $H_s=7.5$ cm, $T_p=1.5$ s, and $h_r=3.1$ cm

transfer function (e.g., Bowers 1977). As the waves propagated over the reef face, energy is transferred from the spectral peak frequency to both lower and higher frequencies with the infragravity energy amplified relative to the offshore gauge. The spectral densities of the reef flat Gauges 7–9 are shown in Fig. 5. Gauge 7 is located directly at the reef crest in an active breaking region and still has a considerable amount of energy around the peak frequency of the incident wave ($f_p=0.67$ Hz). However, the wave energy spectral densities at Gauges 8 and 9, which are located at the middle and end of the reef flat, are dominated by low frequency motions with most of the wave energy at the peak frequency of the incident waves dissipated. The infragravity wave energy is lowest at the reef crest and increases shoreward over the reef flat.

To better understand the infragravity motions over the reef flat, we examine the “raw” nonsmoothed (2-dof) infragravity wave

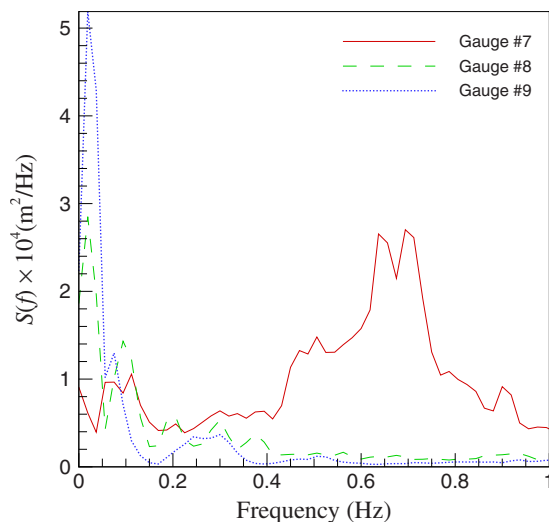


Fig. 5. Wave energy spectra at reef flat Gauges 7–9 for incident waves with $H_s=7.5$ cm, $T_p=1.5$ s, and $h_r=3.1$ cm

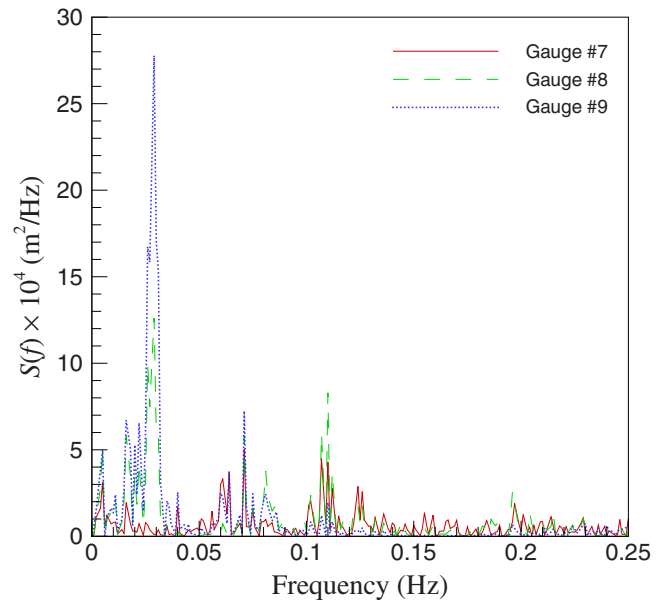


Fig. 6. Nonsmoothed infragravity wave spectra at Gauges 7–9 for incident waves with $H_s=7.5$ cm, $T_p=1.5$ s, and $h_r=3.1$ cm

spectrum in greater detail. The infragravity wave spectra at the reef flat gauges are plotted in Fig. 6 while the runup height spectrum is plotted in Fig. 7. The infragravity wave energy at the reef crest Gauge 7 is not broad banded but occurs in distinct clusters with the largest component at $f \approx 0.07$ Hz which corresponds to the peak frequency of the offshore wave envelope. This is consistent with previous observations of a correlation between infragravity motions in the surf zone and the group structure of the incident short waves (List 1986; Masselink 1995). The infragravity wave spectra at the middle and end of the reef flat (Gauges 8 and 9) and runup height spectrum are dominated by motions at $f \approx 0.029$ Hz ($T \approx 35$ s). There is, however, very little energy at the 35-s period at the reef crest Gauge 7. The 35-s period corre-

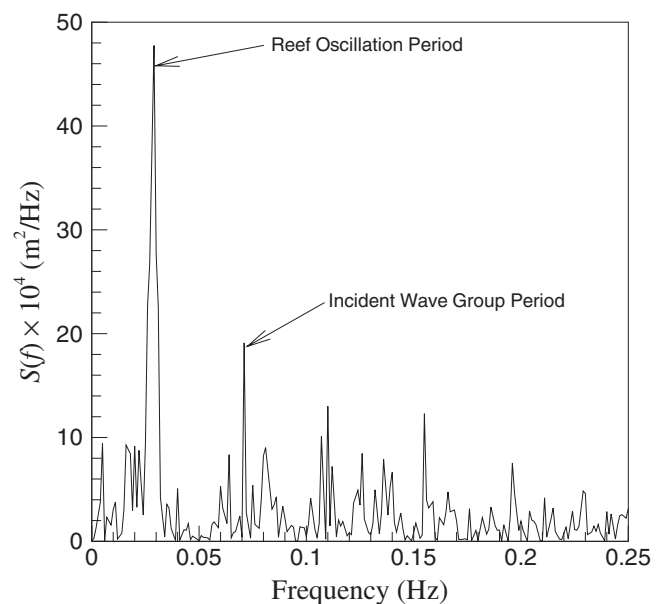


Fig. 7. Nonsmoothed runup energy density spectrum for incident waves with $H_s=7.5$ cm, $T_p=1.5$ s, and $h_r=3.1$ cm

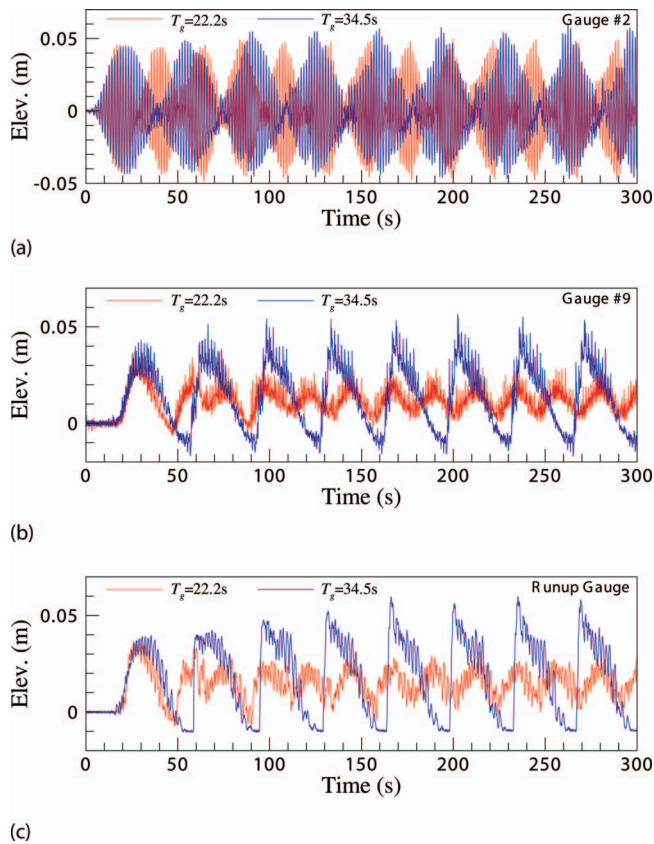


Fig. 8. (Color) Time series at offshore Gauge 2, reef flat Gauge 9, and runup gauge for bichromatic waves with group periods $T_g = 22.2$ and 34.5 s ($h_r = 3.1$ cm)

sponds to the first reef oscillation mode ($n=1$) with a wavelength approximately equal to four times the width of the reef flat if the reef-beach system is considered to be an open basin with natural periods given by

$$T_n = \frac{4l_r}{(2n-1)\sqrt{gh_r}}, \quad n = 1, 2, 3 \dots \quad (15)$$

where $l_r = 4.8$ m is the width of the reef top and $h_r =$ water depth over the reef flat. The first mode has a node at the reef crest and anti-node at the shoreline. The magnitude of the first-mode infragravity wave trapped over the reef flat would thus increase from the reef crest to the shoreline.

Additional experiments were conducted with bichromatic wave trains to elucidate differences between the runup characteristics of the trapped and nontrapped infragravity waves. Two sets of bichromatic waves were generated with the same offshore wave heights $H_1 = H_2 = 0.042$ m but different group periods. The first group period was chosen to match the reef natural period with component frequencies $f_1 = 0.652$ Hz, $f_2 = 0.681$ Hz, and group period $T_g = 1/(f_2 - f_1) = 34.5$ sec, while the second wave train consisted of components with $f_1 = 0.645$ Hz, $f_2 = 0.69$ Hz, and $T_g = 22.2$ s. The time histories of the measured free surface elevation at the offshore Gauge 2, reef-flat Gauge 9, and runup gauge are plotted in Fig. 8 for both sets of bichromatic waves. The incident wave heights for both the resonant and nonresonant bichromatic wave trains are initially similar at the offshore gauge. The runup characteristics of the first group of waves that arrive at the shoreline are also similar. However, the infragravity waves for

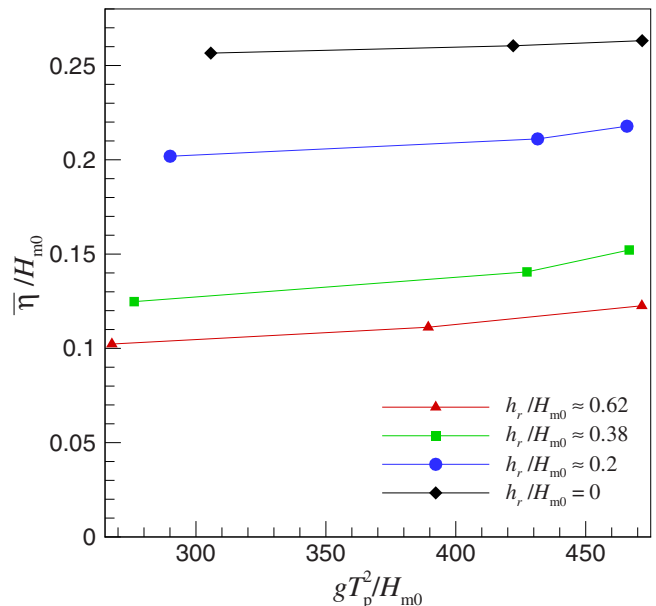


Fig. 9. Variation of wave setup at Gauge 9 with inverse wave steepness parameter for different water levels

the $T_g = 34.5$ s wave group become trapped over the reef flat and gradually build up to resonant oscillations at the shoreline over four group periods.

Several semiempirical formulations have been proposed to predict the runup of irregular waves on planar beaches. In general, the maximum runup height R depends on the incident wave parameters (H_{m0}, T_p), acceleration due to gravity, g , and beach slope, $\tan \beta$

$$R_{\max} = f(H_{m0}, T_p, \tan \beta) \quad (16)$$

Dimensional considerations suggest that the runup height can be written as

$$\frac{R_{\max}}{H_{m0}} = f(\xi) \quad (17)$$

where $\xi = \tan \beta / \sqrt{2\pi H_{m0} / g T_p^2}$ = surf similarity parameter (or Iribarren number). Hunt (1959) suggested a linear dependence of the runup height with surf similarity parameter for broken waves on planar beaches

$$\frac{R_{\max}}{H_{m0}} = \xi \quad (18)$$

Variants of Hunt's formula have been adopted in the *Coastal Engineering Manual* of the U.S. Army Corps of Engineers (Demirbilek and Vincent 2002). For beaches fronted by shallow fringing reefs, the water depth over the reef flat h_r plays an important role in determining the maximum runup height. Gourlay (1996a) investigated the functional dependence of water level setup over coral reefs with relative water level h_r/H_{m0} and wave steepness H_{m0}/gT_p^2 . Since the inverse wave steepness gT_p^2/H_{m0} is directly related to the surf similarity parameter, i.e.,

$$\frac{gT_p^2}{H_{m0}} = \frac{2\pi}{\tan \beta} \xi^2 \quad (19)$$

we plot the variation of the wave setup and runup height against the inverse wave steepness parameter gT_p^2/H_{m0} for different relative water levels. Fig. 9 shows a plot of the nondimensional water

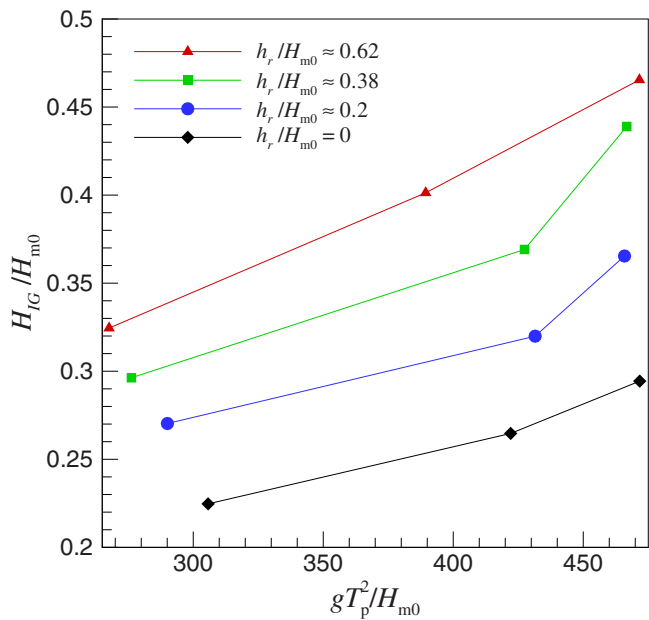


Fig. 10. Variation of infragravity wave height at Gauge 9 with inverse wave steepness parameter for different water levels

level setup over the reef flat (Gauge 9) versus gT_p^2/H_{m0} for different values of h_r/H_{m0} . The wave setup is governed primarily by the water depth over the reef flat with a weak dependence with gT_p^2/H_{m0} . The increase in wave setup with decreasing water level on the reef flat has been previously reported by other investigators (Seelig 1983; Gourlay 1996a) and can be explained using radiation stress theory (Tait 1972; Gourlay 1996b).

The infragravity wave energy over the reef flat was obtained from the wave energy spectrum $S_\eta(f)$ by filtering out frequency components with $f > f_c = 0.25$ Hz. A characteristic infragravity wave height was then obtained as

$$H_{IG} = 4 \sqrt{\int_0^{f_c} S_\eta(f) df} \quad (20)$$

The variation of the nondimensional infragravity wave height with inverse wave steepness parameter is shown in Fig. 10. In contrast to the water level setup, the infragravity wave energy increases with increasing water level over the reef flat. The infragravity energy also shows a stronger dependence on the inverse wave steepness parameter.

The nondimensional maximum wave runup height for different relative water levels is plotted in Fig. 11 as a function of gT_p^2/H_{m0} . The wave runup includes a static contribution from the mean water level setup and a dynamic contribution from oscillations at infragravity frequencies. Although the wave setup decreased with increasing water level, the wave runup increased with increasing water level due to a more dominant contribution from infragravity oscillations. With the exception of data points for $h_r/H_{m0} \approx 0.2$, the runup heights increased linearly with gT_p^2/H_{m0} . This would seem to suggest a quadratic dependence of maximum runup height with surf similarity parameter for breaking waves on fringing reef profiles

$$\frac{R_{\max}}{H_{m0}} = a\xi^2 + b \quad (21)$$

where a and b depend on the relative water level h_r/H_{m0} . This differs from the linear dependence of runup height with surf simi-

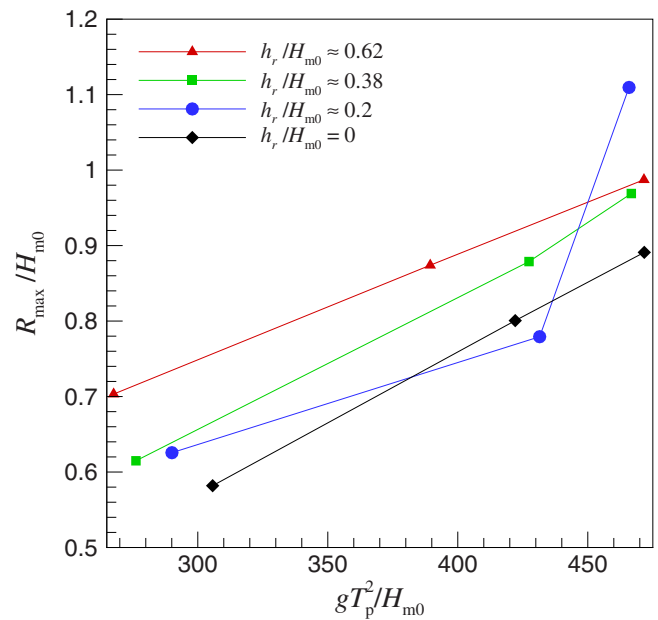


Fig. 11. Variation of maximum wave runup height with inverse wave steepness parameter for different water levels

ilarity parameter in Hunt's formula. A quadratic variation of runup height with surf similarity parameter was also obtained by Raubenheimer and Guza (1996) by including the effect of breaking in Carrier and Greenspan's (1958) analytical solution for long wave runup.

Model-Data Comparisons

The nonlinear Boussinesq wave model described earlier makes several simplifying assumptions that limit its ability to reproduce

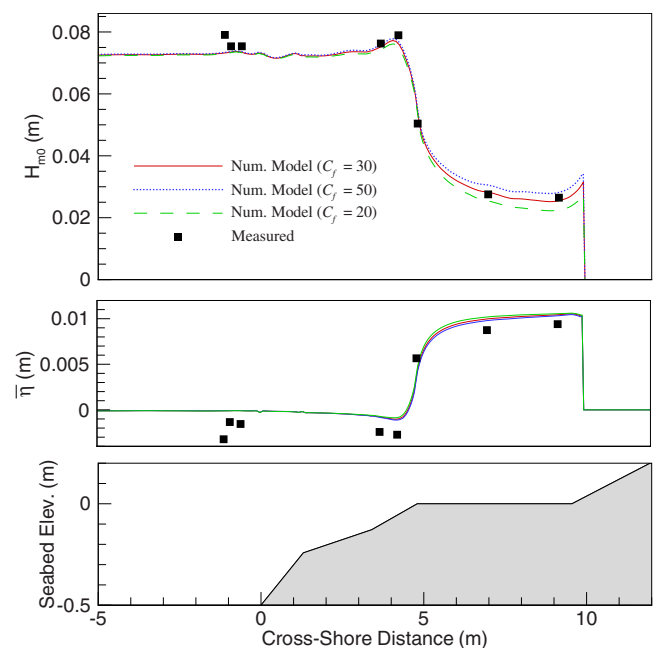


Fig. 12. Measured and predicted significant wave height and mean water level variation for incident waves with $H_{m0} = 0.075$ m, $T_p = 1.5$ s, and $h_r = 3.1$ cm

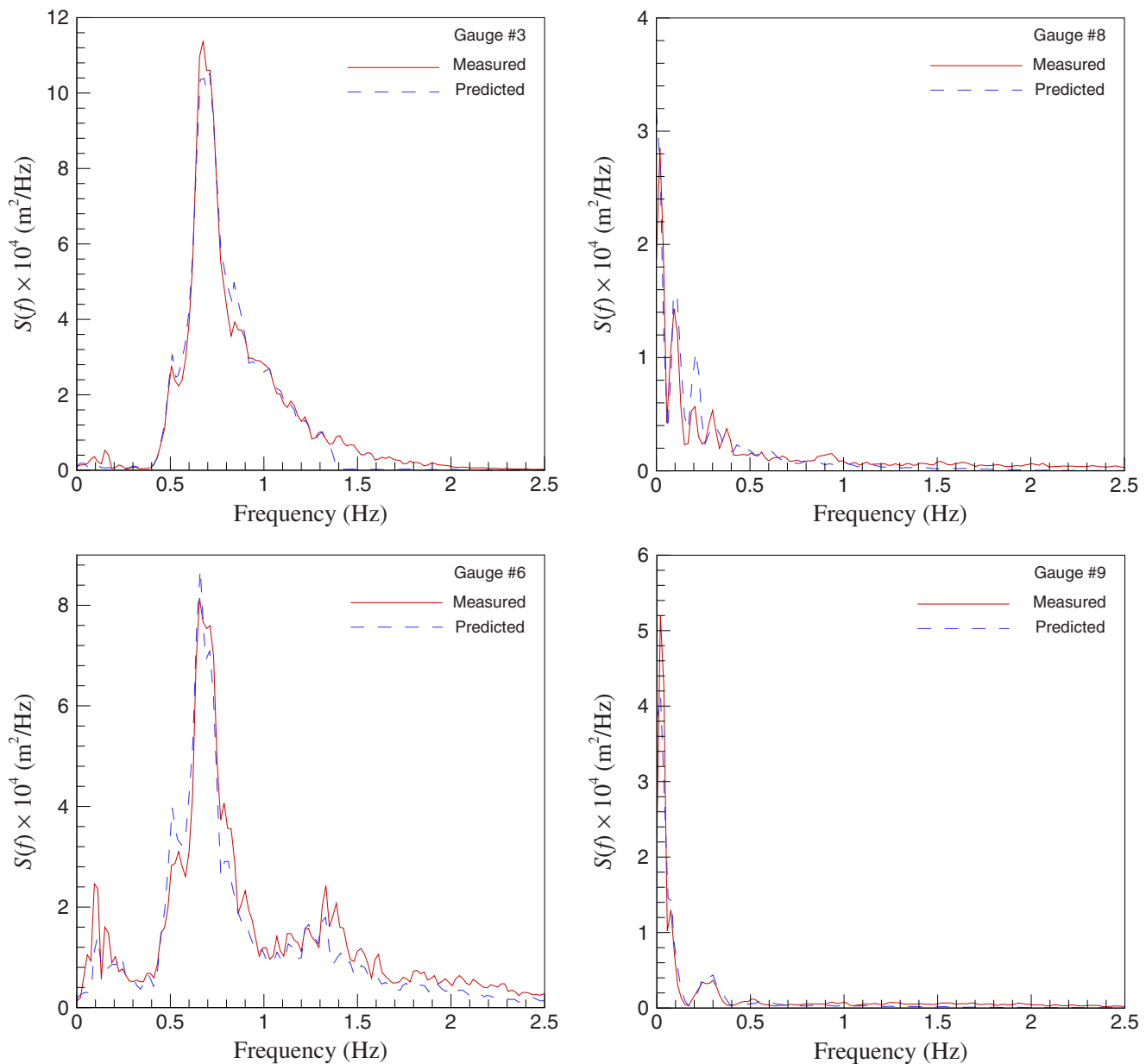


Fig. 13. Comparison of measured and predicted wave spectra at selected gauges for incident waves with $H_s=7.5$ cm, $T_p=1.5$ s, and $h_r=3.1$ cm

the observed complex nonlinear evolution of waves over shallow fringing reefs. The Taylor series expansion of the velocity field [Eq. (3)] requires the second-order terms to be an order of magnitude smaller than the first-order term. This imposes a dispersive limit on the shortest wavelength λ relative to the water depth h , $(h/\lambda)^2 \ll 1$, and bottom slope relative to frequency dispersion parameter, $\partial h/\partial x \ll \lambda/h$. The neglected higher-order nonlinear dispersive terms also lead to an underprediction of bound long waves in intermediate water depths (Nwogu 1993). Viscous effects related to wave breaking and bottom friction are also parameterized in the Boussinesq model. Since viscous parametrizations represent simplifications of complex turbulent flow processes, we investigated the ability of the parametrized Boussinesq model to describe physics of wave energy dissipation, infragravity wave motions, and wave runup across fringing reef profiles through comparisons of numerical model predictions with experimental data.

Numerical simulations were performed for the irregular wave condition described earlier with $H_{m0}=7.5$ cm, $T_p=1.5$ s, and $h_r=3.1$ cm. The measured water surface elevation time series at Gauge 1 was used to derive velocity boundary conditions for the numerical model. The numerical model was configured to reproduce the experimental setup shown in Fig. 1 with an internal wavemaker placed at the location of Gauge 1. A 10-m wide damping layer was placed behind the internal wavemaker to effectively absorb seaward-propagating long waves. The simulations were carried out using grid spacing $\Delta x=0.05$ m, time step size $\Delta t=0.01$ s, and minimum flooding depth $\delta_{\min}=H_{m0}/1,000$.

The rate of wave energy dissipation in the numerical model is controlled by the turbulent length scale, l_r , and bottom friction factor f_w or Chezy coefficient $C_f=\sqrt{2g/f_w}$. Since wave breaking is localized near the reef crest, the turbulent length scale was selected to match the initial rate of wave height decay near the

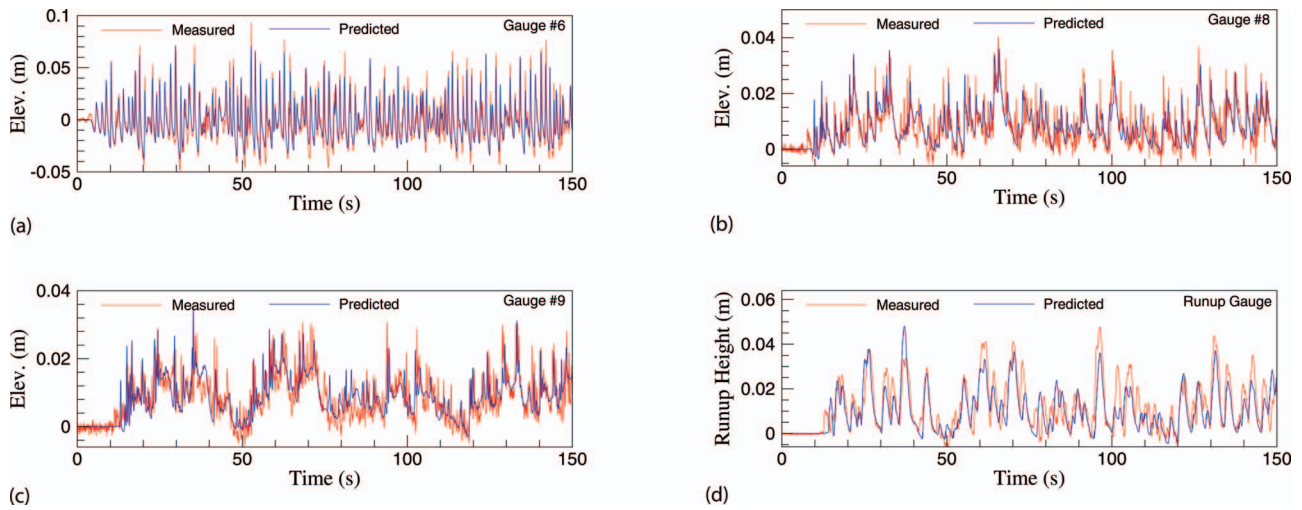


Fig. 14. (Color) Comparison of measured and predicted surface elevation time histories at selected gauges for incident waves with $H_s = 7.5$ cm, $T_p = 1.5$ s, and $h_r = 3.1$ cm

reef crest with an optimal value approximately equal to the offshore significant wave height. The measured and model-predicted significant wave height variation and mean water level setup across the reef-slope topography are plotted in Fig. 12 for three different values of the Chezy coefficient ($C_f = 20, 30, 50$). As expected, the predicted heights over the reef flat were sensitive to the magnitude of the bottom friction coefficient with variations of the order of $\pm 10\%$ for Chezy coefficients ranging from 20 to 50. The breaking parameterization is able to capture the rapid dissipation of energy and the associated setup of the mean water level. The decrease in the mean water level offshore of the reef in the measured data was due to the use of a closed laboratory flume with no recirculation of the water pumped onto the reef. The Boussinesq model used a Rayleigh damping term in the mass conservation equation [Eq. (1)] which acts to maintain a zero-mean water level in the offshore region.

Spectral wind-wave models that solve the energy balance equation with a dissipative term for breaking can be tuned to predict wave height variation across the reef profiles (e.g., Gerritsen 1980). However, these models either exclude or parameterize

the nonlinear triad interactions responsible for the cross-spectral transfer of energy to infragravity modes. Boussinesq models have the advantage of including the effect of nonlinear wave-wave interactions, although limited by the truncation of higher-order nonlinear dispersive terms. We next compare in Fig. 13 the measured and predicted spectral densities (60-dof) at an offshore Gauge 3, reef-face Gauge 6, and gauges located at the middle and end of the reef flat (Gauges 8 and 9). The measured spectrum at Gauge 6 just offshore of the reef crest shows the growth of bound subharmonics and superharmonics. The predicted spectrum matches the observed spectrum reasonably well although it underestimated the low-frequency peak at $f \approx 0.1$ Hz and some of the high-frequency energy that are beyond the dispersive limit of the model. The wave spectra at the reef flat Gauges 8 and 9 are dominated by infragravity oscillations with most of the energy around the peak frequency of the incident waves dissipated by breaking. Overall, the Boussinesq model is able to reproduce the major features of the low frequency oscillations over the reef flat. The breaking parameterization preferen-

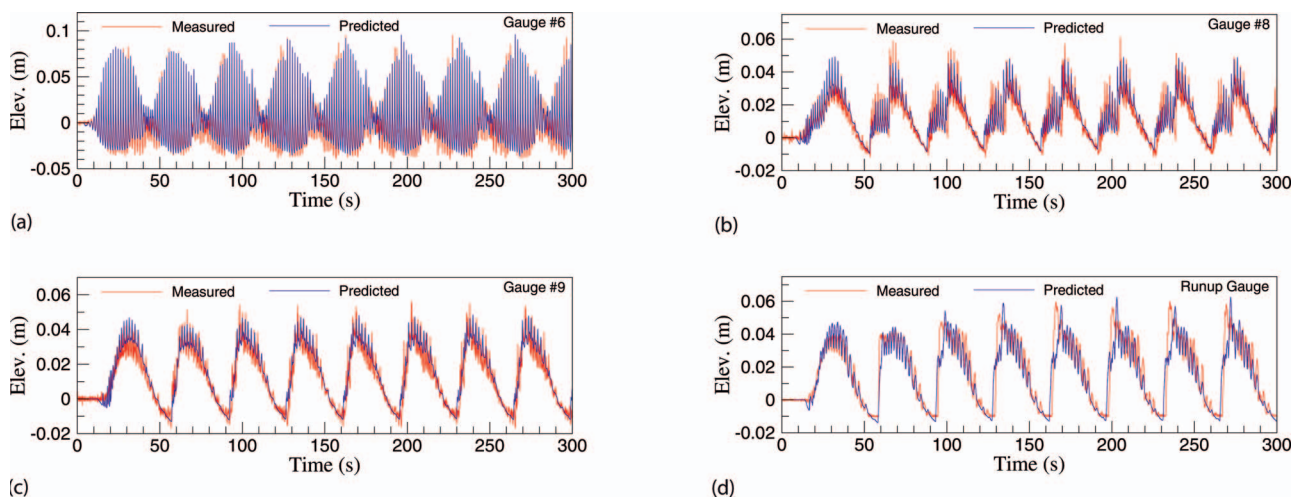


Fig. 15. (Color) Comparison of measured and predicted time series at selected gauges for bichromatic waves with group period $T_g = 34.5$ s ($h_r = 3.1$ cm)

tially dissipates the high-frequency energy with the lower frequency component becoming dominant over the reef flat.

The predicted surface elevation time histories are compared to the measured data in Fig. 14. The numerical model is able to describe the nonlinear steepening and highly asymmetric profile of postbreaking waves in relatively shallow depths and the amplitude and phasing of the low-frequency motions over the reef flat. The runup predictions are also reasonable, although there are slight discrepancies in details of the fluctuations. Given that viscous effects related to wave breaking is parameterized in the Boussinesq model, we cannot expect the model to capture fine details of post-breaking waves on a wave-by-wave basis. The adopted breaking criterion, for example, is based on the ratio of the water particle velocity at the crest to the phase velocity. The phase velocity is computed using linear theory and the average zero-crossing period of the incident wave train. This might lead to an earlier or later initiation of breaking for individual waves, depending on the individual wave frequencies and amplitudes.

We also simulated the trapped infragravity test case for bichromatic incident waves with $H_1=H_2=0.042$ m, $f_1=0.652$ Hz, $f_2=0.681$ Hz, and group period equal to the first reef oscillation period. The simulation parameters were identical to that used earlier for the irregular test case. The model-predicted time histories of the free surface elevation on the reef face (Gauge 6), reef flat (Gauges 8 and 9), and runup gauges are presented in Fig. 15. The Boussinesq model is able to accurately describe nonlinear wave shoaling over the reef face, wave breaking near the reef crest, and resonant infragravity oscillations over the reef flat and shoreline. Since most of the short-period waves are dissipated by breaking at the reef crest, the bound long wave energy would be negligible over the reef flat. The question then arises as to the mechanism responsible for the generation of free infragravity waves that propagate shoreward over the reef flat before being reflected at the shoreline. Longuet-Higgins and Stewart (1964) suggested that bound long waves are released as free waves at the break point but did not clarify the release mechanism. Symonds et al. (1982) hypothesized that free seaward and shoreward propagating long waves are directly generated at the break point due to group-induced oscillations of the breaking location. The Boussinesq model does not have any explicit mechanism for releasing or generating free long waves at the break point but implicitly includes the radiation stress and an eddy-viscosity-based dissipation term. The successful reproduction of the amplitude and phasing of free long wave motions over the reef flat would seem to suggest that the mechanism for the release of bound waves as free waves at the break point is simply the preferential dissipation of the short-period wave energy.

Concluding Remarks

Laboratory experiments have been conducted to investigate the transformation of irregular waves over fringing coral reefs and wave runup at the shoreline. Most of the wave energy in the incident-wave frequency band is dissipated by breaking within a few wavelengths of reef crest, resulting in long-period (infragravity) oscillations dominating the fluid motions over the reef flat and shoreline. The dominant infragravity mode is the first reef oscillation mode with a wavelength approximately equal to four times the width of the reef flat. This component is trapped over the reef flat and resonantly amplified at the shoreline leading to larger runup heights. Numerical simulations were conducted with a Boussinesq wave model to evaluate its ability to describe the

complex wave transformation process over the reef. The model-predicted post-breaking wave heights and setup over the reef flat were sensitive to the semi-empirical coefficients of the parameterized turbulent processes. Overall, the model performed reasonably well and was able to describe not only the variation of the significant wave height and mean water level across the reef profile but also complex changes to the wave spectrum due to wave breaking, nonlinear energy transfer to the infragravity band, and trapped infragravity oscillations over the reef flat. The model would be highly useful for predicting coastal flooding over reef-fronted coasts.

Acknowledgments

This work was supported by the Surge and Wave Island Modeling Studies (SWIMS) and Navigation Systems programs of the U.S. Army Engineer Research and Development Center. Permission to publish this paper was granted by the Chief of Engineers, U.S. Army Corps of Engineers.

References

- Battjes, J. A., and Janssen, J. P. F. M. (1978). "Energy loss and set-up due to breaking of random waves." *Proc., 16th Int. Conf. Coastal Eng., ASCE*, Reston, Va., 569–587.
- Bowers, E. C. (1977). "Harbour resonance due to set-down beneath wave groups." *J. Fluid Mech.*, 79, 71–92.
- Carrier, G. F., and Greenspan, H. P. (1958). "Water waves of finite amplitude on a sloping beach." *J. Fluid Mech.*, 4, 97–109.
- Demirbilek, Z., Nwogu, O. G., and Ward, D. L. (2007). "Laboratory study of wind effect on runup over fringing reefs. Report 1: Data report." *Coastal and Hydraulics Laboratory Technical Rep. No. ERDC/CHL-TR-07-4*. U.S. Army Engineer Research and Development Center, Vicksburg, Miss.
- Demirbilek, Z., and Vincent, C. L. (2002). "Chapter III: Wave mechanics. Part II: Hydrodynamics. Engineer manual 1110–2-1100." *Coastal engineering manual*, U.S. Army Corps of Engineers, Washington, D.C.
- Gerritsen, F. (1980). "Wave attenuation and wave set-up on a coastal reef." *Proc., 17th Int. Conf. Coastal Eng., ASCE*, Reston, Va., 444–461.
- Gourlay, M. R. (1996a). "Wave set-up on coral reefs. 1. Set-up and wave-generated flow on an idealized two dimensional horizontal reef." *Coastal Eng.*, 27, 161–193.
- Gourlay, M. R. (1996b). "Wave set-up on coral reefs. 2. Set-up on reefs with various profiles." *Coastal Eng.*, 28, 17–55.
- Heitner, K. L., and Housner, G. W. (1970). "Numerical model for tsunami runup." *J. Wtrwy., Harb. and Coast. Engrg. Div.*, 96(3), 701–719.
- Hunt, I. A. (1959). "Design of seawalls and breakwaters." *J. Wtrwy., Harb. and Coast. Engrg. Div.*, 85, 123–152.
- Jaffe, B. E., and Richmond, B. M. 1993. "Overwash variability on the shoreline of Guam during Typhoon Russ." *Proc., 7th Int. Coral Reef Symp.*, University of Guam Press, UOG Station, Guam, 257–264.
- Kennedy, A. B., Chen, Q., Kirby, J. T., and Dalrymple, R. A. (2000). "Boussinesq modeling of wave transformation, breaking, and runup. Part I: 1D." *J. Waterway, Port, Coastal, Ocean Eng.*, 126(1), 39–47.
- Kobayashi, N., Otta, A. K., and Roy, I. (1987). "Wave reflection and runup in rough slopes." *J. Waterway, Port, Coastal, Ocean Eng.*, 113(3), 282–297.
- Lee, T. T., and Black, K. P. (1978). "The energy spectra of surf waves on a coral reef." *Proc., 16th Int. Conf. Coastal Eng., ASCE*, Reston, Va., 588–608.
- List, J. H. (1986). "Wave groupiness as a source of nearshore long

- waves." *Proc., 20th Int. Conf. Coastal Eng.*, ASCE, Reston, Va., 497–511.
- Liu, P. L.-F., and Orfila, A. (2004). "Viscous effects on transient long-wave propagation." *J. Fluid Mech.*, 520, 83–92.
- Longuet-Higgins, M. S., and Stewart, R. W. (1964). "Radiation stress in water waves: Physical discussion with applications." *Deep-Sea Res.*, 11, 529–562.
- Madsen, P. A., Sorensen, O. R., and Schaffer, H. A. (1997). "Surf zone dynamics simulated by a Boussinesq type model. Part I: Model description and cross-shore motion of regular waves." *Coastal Eng.*, 32, 255–287.
- Massel, S. R., and Gourlay, M. R. (2000). "On the modelling of wave breaking and set-up on coral reefs." *Coastal Eng.*, 39, 1–27.
- Masselink, G. (1995). "Group bound long waves as a source of infragravity energy in the surf zone." *Cont. Shelf Res.*, 15, 1525–1547.
- McDonald, B. E., and Witting, J. M. (1984). "A conservation law related to Kelvin's circulation theorem." *J. Comput. Phys.*, 56, 237–243.
- Munk, W. H., and Sargent, M. C. (1948). "Adjustment of Bikini Atoll to ocean waves." *Trans., Am. Geophys. Union*, 29, 855–860.
- Nakaza, E., and Hino, M. (1991). "Bore-like surf beat in a reef zone caused by wave groups of incident short period waves." *Fluid Dyn. Res.*, 7, 89–100.
- Nakaza, E., Tsukayama, S., and Hino, M. (1991). "Bore-like surf beat on reefs." *Proc., 22nd Int. Conf. Coastal Eng.*, ASCE, Reston, Va., 743–756.
- Nwogu, O. (1993). "Alternative form of Boussinesq equations for near-shore wave propagation." *J. Waterway, Port, Coastal, Ocean Eng.*, 119(6), 618–638.
- Nwogu, O., and Demirbilek, Z. (2001). "BOUSS-2D: Boussinesq wave model for coastal regions and harbors." *Technical Rep. No. ERDC/CHL TR-01-25*. Coastal and Hydraulics Laboratory, U.S. Army Engineer Research and Development Center, Vicksburg, Miss.
- Nwogu, O. G. (2009). "Interaction of finite-amplitude waves with vertically sheared current fields." *J. Fluid Mech.*, 627, 179–213.
- Ogg, J. G., and Koslow, J. A. (1978). "The impact of typhoon Pamela, 1976, on Guam's coral reefs and beaches." *Pacific Science*, 32, 105–118.
- Raubenheimer, B., and Guza, R. T. (1996). "Observations and predictions of runup." *J. Geophys. Res.*, 101, 25,575–25,587.
- Seelig, W. (1983). "Laboratory study of reef-lagoon system hydraulics." *J. Waterway, Port, Coastal, Ocean Eng.*, 109(4), 380–391.
- Skotner, C., and Apelt, C. J. (1999). "Application of a Boussinesq model for the computation of breaking waves. Part II: Wave-induced set-down and setup on a submerged coral reef." *Ocean Eng.*, 26, 927–947.
- Smagorinsky, J. (1963). "General circulation experiments with the primitive equations." *Mon. Weather Rev.*, 91, 99–164.
- Svendsen, I. A. (1984). "Wave heights and set-up in a surf zone." *Coastal Eng.*, 8, 303–329.
- Symonds, G., Black, K. P., and Young, I. R. (1995). "Wave-driven flow over shallow reefs." *J. Geophys. Res.*, 100, 2,639–2,648.
- Symonds, G., Huntley, D., and Bowen, A. (1982). "Two dimensional surf-beat: Long wave generation by a time-varying break point." *J. Geophys. Res.*, 87, 492–498.
- Tait, R. J. (1972). "Wave setup on coral reefs." *J. Geophys. Res.*, 77, 2207–2211.
- Von Neumann, J., and Richtmyer, R. (1950). "A method for the numerical calculation of hydrodynamic shocks." *J. Appl. Phys.*, 21, 232–237.
- Zelt, J. A. (1991). "The runup of nonbreaking and breaking solitary waves." *Coastal Eng.*, 15, 205–246.